metals

MDPI

Article

Simulation and Experimental Comparison of Laser Impact Welding with a Plasma Pressure Model

Sepehr Sadeh, Glenn H. Gleason, Mohammad I. Hatamleh, Sumair F. Sunny, Haoliang Yu, Arif S. Malik * and Dong Qian

Department of Mechanical Engineering, Erik Jonsson School of Engineering and Computer Science, The University of Texas at Dallas, 800 W. Campbell Rd., Richardson, TX 75080, USA; sepehr.sadeh@utdallas.edu (S.S.); glenn.gleason@utdallas.edu (G.H.G.); mohammad.hatamleh@utdallas.ed (M.I.H.); sumair.sunny@utdallas.edu (S.F.S.); haoliang.yu@utdallas.edu (H.Y.); dong.qian@utdallas.edu (D.Q.)

* Correspondence: arif.malik@utdallas.edu; Tel.: +1-972-883-4550

Received: 7 October 2019; Accepted: 29 October 2019; Published: 7 November 2019

check for updates

Abstract: In this study, spatial and temporal profiles of an Nd-YAG laser beam pressure pulse are experimentally characterized and fully captured for use in numerical simulations of laser impact welding (LIW). Both axisymmetric, Arbitrary Lagrangian-Eulerian (ALE) and Eulerian dynamic explicit numerical simulations of the collision and deformation of the flyer and target foils are created. The effect of the standoff distance between the foils on impact angle, velocity distribution, springback, the overall shape of the deformed foils, and the weld strength in lap shear tests are investigated. In addition, the jetting phenomenon (separation and ejection of particles at very high velocities due to high-impact collision) and interlocking of the foils along the weld interface are simulated. Simulation results are compared to experiments, which exhibit very similar deformation and impact behaviors. In contrast to previous numerical studies that assume a pre-defined deformed flyer foil shape with uniform initial velocity, the research in this work shows that incorporation of the actual spatial and temporal profiles of the laser beam and modeling of the corresponding pressure pulse based on a laser shock peening approach provides a more realistic prediction of the LIW process mechanism.

Keywords: high-velocity impact welding; laser impact welding; finite element simulation; experimental analysis

1. Introduction

High-velocity impact welding (HVIW) methods are rapidly gaining popularity in joining of similar and dissimilar metals. Compared to conventional fusion-based welding techniques, impact welding is very rapid and could be applied to a wide variety of metals. The primary advantage of impact welding is that metals are joined due to the high impact, thus achieving melting temperatures is not required. Therefore, metals with widely differing melting temperatures and mechanical properties can be welded by impact alone, hence, avoiding the formation of brittle intermetallic compounds. During the short impact welding process, and depending on materials, their surface morphologies, and impact angle and velocity, material flow 'waves' that lead to interlocking and bonding may be observed at the impact interface. Depending on the end-use application and dimensions of the impacting metals, various means have been used for impact generation. From larger to smaller scale, the four main impact-driven joining methods are Explosive Welding (EXW), Magnetic Pulse Welding (MPW), Vaporizing Foil Actuator Welding (VFAW), and LIW, named according to their source of impact upon launching a flyer plate towards a target (base) plate. The high-impact pressure loads are generated in EXW, MPW, VFAW, and LIW, respectively, due to explosive detonation, large magnetic field, high voltage rapid vaporization of a metal foil, and surface ablation of a metal by a focused laser beam.

In the past few decades, both experimental and numerical investigations have been conducted into the aforementioned processes. In previous numerical studies on HVIW of both similar and dissimilar metals, an initial flyer velocity, impact angle, deformed flyer shape (at impact), and corresponding simplified boundary conditions have been assumed. These numerical studies have focused on mimicking the material jetting and morphology of the weld interface. In addition, only two-dimensional simulations of small sections of the entire model have been considered even though the actual dimensions of the flyer and target plates, as well as their boundary conditions, are important to accurately capture the deformed shapes prior to and during impact.

In consideration of the above, we briefly introduce the various HVIW methods and a discussion of related experimental and numerical studies reported in the literature.

1.1. Explosive Welding

In EXW, a controlled detonation provides the source of the high-velocity impact. The explosion accelerates a flyer plate towards a base (target) plate, leading to a weld due to high-velocity collision. Since its discovery in 1957 [1], EXW has been studied by many researchers. Szecket and Mayseless [2] reported on methods of introducing an 'artificial disturbance' to stabilize the wave formation at the weld interface when joining similar metals (copper to copper, and mild steel to mild steel). Mousavi and Al-Hassani [3] designed a physical experiment to mimic the conditions of explosive welding using a pneumatic gun. They performed oblique welding of 3 mm thick flyers of copper, stainless steel, titanium, and zirconium to 30 mm thick base plates of mild steel. Assuming a wide range of constant initial impact angles and flyer velocities, they performed 2D Eulerian simulations of the process to show spallation and jetting of material at the collision interface. Aside from Eulerian simulation methods, meshfree methods such as the Material Point Method (MPM) and Smooth Particle Hydrodynamics (SPH) have also been used to simulate EXW. For example, Wang et al. [4] utilized MPM to model the welding of a 10 mm thick copper flyer plate to a 50 mm thick steel base plate driven by the explosion of ammonium nitrate. Their method did not simulate the formation of a wavy interface but did capture the 'flight' shape of the flyer. Wang et al. [5] simulated EXW of aluminum, steel, and copper flyers against titanium base plates using SPH, but with constant initial flyer velocities assumed. They observed waves having larger wavelengths and greater amplitudes in the collision of stainless steel and titanium compared to aluminum and titanium. Zhang et al. [6] implemented a density-adaptive SPH technique to model EXW, including the detonation of the explosive. They reported that the attainment of requisite impact angles in a parallel flyer/target setup is more challenging compared to oblique orientations.

1.2. Magnetic Pulse Welding

In MPW, the sudden discharge of a capacitor generates very high electric currents through a coil, leading to a very high magnetic field pressure that accelerates toward one another the parts to be welded. Welding of a wide range of similar and dissimilar materials in different MPW configurations have been reported. For example, Okagawa and Aizawa [7] proposed a parallel MPW configuration that led to seam welds between 1 mm thick aluminum sheets. They experimentally studied the seam weld shearing strength and observed its dependence on the kinetic energy of the sheets before the collision and magnetic pressure after the collision. Watanabe et al. [8] obtained lap joints for aluminum flyer plates and iron, nickel, and copper base plates. They reported that exceeding a certain level of discharge energy resulted in a decrease in amplitude and wavelength of material interflow at the weld interface. Lee et al. [9] produced lap joints between 1.2 mm thick aluminum flyer plates and 1 mm thick low-carbon steel plates using MPW. They observed a slight flattening of the grains of aluminum plates in the vicinity of the weld after impact, but no change was apparent in the grain structure of the steel plates. Their nano-indentation hardness tests revealed increased hardness in the intermediate layer between the plates. Ben-Artzy et al. [10] showed that, in tubular MPW joints, reflected shock waves generate interference waves along the weld interface, and that the wavelength of interference waves is proportional to the free path of the shock wave propagation (the first path between front face and back surface) on the interior side of the weld. Göbel et al. [11] made a comparison between the physics involved in EXW and MPW. They reported that in MPW the impact velocity and angle changes along the weld, and that wave creation is possible at lower velocities in MPW compared to EXW. This allows for different welding windows (in terms of impact angle and velocity) in MPW and EXW. Raoelison et al. [12] performed an Eulerian simulation of MPW assuming a linear flyer velocity distribution having a mean value of 600 m/s for aluminum workpieces. They predicted thermomechanical material flow in the form of particle jetting. Cui et al. [13] proposed a method for MPW of 1.4 mm thick carbon-fiber-reinforced plastic and 1 mm thick aluminum tubes. They numerically imitated the MPW process using a coupled electromagnetic and mechanical simulation with constant stress elements.

1.3. Vaporizing Foil Actuator Welding

In VFAW, a sudden capacitor-discharge generates a very high current through a thin conductor foil, vaporizing it almost instantaneously. This creates a very high-pressure plasma, which accelerates the flyer plate towards the target plate. The technique was introduced by Vivek et al. [14] in 2013. They successfully welded copper to titanium, copper to steel, aluminum to copper, aluminum to magnesium, and titanium to steel. Moreover, they quadrupled the weld strength of the titanium/steel combination by introducing a thin nickel interlayer. Hahn et al. [15] attempted an experimental comparison of VFAW and MPW and achieved success only for VFAW. Using the same charging energies of the pulse generator, with VFAW they reached velocities three times those for MPW. Vivek et al. [16] demonstrated two VFAW experiments to join copper sheets with 3 mm thick zirconium-based bulk metallic glass (BMG). In one experiment, the 0.5 mm thick copper sheet was directly launched towards the BMG, resulting in a straight welded interface. In the other experiment, a 0.5 mm thick titanium sheet was first launched towards a 0.25 mm thick copper sheet, consequently launching it towards the BMG, which resulted in a wavy weld interface and no devitrification of the BMG. Nassiri and Kinsey [17] created 2D simulations for VFAW of 2 mm thick flyer and 3 mm thick base plates of aluminum using ALE and SPH methods. In both methods, an initial constant flyer velocity and impact angle were assumed. While the SPH method was able to simulate material jetting, it was found to be less accurate compared to ALE. Nassiri et al. [18] conducted a similar comparison study for VFAW of 0.5 mm thick titanium flyer and 1 mm thick copper plates. They validated the ALE and SPH simulation results through VFAW experiments. ALE was deemed incapable of mimicking material vorticities. Chen et al. [19] machined slanted grooves in 6.3 mm thick steel plates at different angles ranging from 8 to 28 degrees and joined them to 0.508 mm thick aluminum flyers using VFAW. They used this technique to control the impact angle, and thus obtained various morphologies at the weld interface. In a separate study [20] that implemented this procedure, aluminum flyer plates of the same thickness were welded to 1.905 mm thick titanium plates. Gupta et al. [21] applied the same technique and similar foil thicknesses in VFAW of copper to titanium, and vice versa. They created an explicit thermomechanical Eulerian simulation with no slip in contact of Eulerian parts but again assuming a constant initial flyer velocity. It was shown that for capture of interfacial waves, sufficient mesh refinement must be implemented. Groche et al. [22] designed an experiment for process window acquisition in HVIW. They used 2 mm thick aluminum workpieces and reached total normal impact velocities up to 262 m/s (131 m/s for each workpiece). It was shown that in cases where the collision point velocity exceeds the speed of sound in aluminum, jetting would not occur, resulting in no bonding.

1.4. Laser Impact Welding

LIW was patented by Daehn and Lippold [23] in 2011. Similar to laser shock peening, a focused laser beam is used to ablate a sacrificial layer, which is placed on the surface of a metal flyer foil.

Rapid vaporization of this ablative layer creates a high-pressure plasma. By using a transparent overlay, the plasma is confined to further increase its pressure. The plasma generates shock waves and accelerates the flyer towards the target metal. Upon collision, jetting and interlocking of the foils occur along a weld interface. Since the deformation of the flyer in LIW is a direct consequence of the shock pressure load generated by the intense laser pulse, there likely exist large velocity gradients amongst regions of the flyer foil upon laser incidence, depending on the spatial profiles of the laser beam and associated pressure pulse. Furthermore, the temporal profiles of the laser pulse and corresponding pressure load further determine the nature of and time to impact in LIW. Thus, assuming a single-valued initial flyer velocity in the simulation of LIW neglects the effects of spatial and temporal profiles of the laser pulse and its plasma pressure load. On that premise, a review of the experimental and numerical studies of LIW follows.

As reported in the literature, successful welds of similar and dissimilar metal foils have been achieved by LIW. Wang et al. [24] used aluminum flyers to investigate the effect of transparent overlay material and laser spot size on the weld quality. They welded nickel flyer (50 μm thick) and base plates using flat and corrugated surfaces on the base. Corrugated base plates provided greater surface area for welding, but large impact angles resulted in no bonding. In a separate experiment using Photonic Doppler Velocimetry (PDV), they revealed that the maximum flyer velocity was achieved within 0.2 μs after impact and in less than 30 μm displacement from the initial position. In addition, they welded 25.4 μm thick aluminum flyer foils to 75 μm thick titanium base foils [25]. It was found that separation of black paint in the ablated area renders it a more suitable ablative layer than black tape. They further studied the effects of laser spot size, the gap between the aluminum flyer and titanium target foils, flyer thickness (from 50 to 250 μm), and transparent overlay material on the weld strength and area [26]. The weld strength and area were evaluated using peel tests and voltage drop measurements [27] across the welds, respectively. It was shown that increasing laser fluence increases the impact velocity (measured by PDV) until the ablative layer reaches its energy absorption limit. It was revealed that by increasing the laser spot size, and thus decreasing the laser fluence, achieving a successful weld becomes more difficult. However, welds achieved by larger spot sizes resulted in greater weld strength and area compared to those achieved by smaller spot sizes. In addition, smaller spot sizes resulted in a greater number of waves with higher amplitude and shorter wavelength on the weld interface. Wang et al. [28] studied the effect of laser fluence on weld interface morphology during oblique LIW of 0.1 mm thick aluminum flyer foils to aluminum and copper base foils of the same thickness. While the authors have reported the laser pulse energy values, it is vital to note that the laser-induced effects heavily depend on the laser spot size among other parameters such as laser wavelength, pulse duration, and the irradiated material [29]. For instance, using the same laser pulse energy, laser impact might generate ultrasounds or shock waves depending on the laser spot size, pulse duration, etc. Superior results (for laser spot size of 6 mm and impact angle of 20 degrees) were obtained at laser fluences of 13.44, 14.15, and 14.85 J/cm^2 when they welded 0.05 mm thick sheets of aluminum and copper flyers to 0.1 mm thick sheets of aluminum base foils [30]. It was found that doubling and tripling the standoff distance between the foils increased the weld diameter by 50% and 83%, respectively. Furthermore, they numerically simulated LIW using the SPH technique in a 2D domain. A constant initial velocity and arc shape in the flyer plate was assumed and showed that increasing the standoff distance resulted in a narrower but taller springback region. The boundary condition applied to the base plate in the numerical model was different from the experimental conditions. In the experiment, the base plate was placed on a back-support while it was left free at the bottom in the numerical simulation. Using the same numerical method and boundary conditions, they simulated LIW of 0.03 mm thick aluminum and titanium flyer plates to 0.1 mm thick copper base plates [31]. Springback of the foils, spallation in the base plate, the jetting, and the wavy interface was simulated and found to be similar to the experimental results. Numerical simulation also revealed that the jetting was mainly produced from a very thin layer of the flyer plate. The numerical simulation was also used to compare LIW of 0.05 mm thick aluminum flyer plates to steel base plates of the same thickness and vice versa [32]. It was shown that using aluminum as the flyer and steel as the target resulted in more successful welds compared to the case where the roles were interchanged. More importantly, swapping the materials changed the direction of wave formation with reference to the impact weld direction. In performing LIW of 0.03 mm thick aluminum flyer plates to 0.08 mm thick brass target plates [33], the authors showed that by increasing the laser fluence, the melting and thus formation of intermetallic compounds was increased, but so did the amplitude and wavelength of the weld interface waves, and the effect of the latter overcame that of the former. Therefore, overall the bond strength was increased with increasing laser fluence. In another experimental work, the authors achieved LIW of 0.03 mm thick crystalline copper flyers to 0.028 mm thick Fe-based metallic glass targets [34]. Copper foil was annealed and attained a finer grain structure prior to LIW. Increased nanoindentation hardness was observed in the copper, the weld interface, and the metallic glass after impact. No crystallization occurred due to LIW and the metallic glass retained an amorphous microstructure after bonding (tested and confirmed only for 1.5 mm laser spot diameter and 47.25 J/cm^2 laser fluence). Liu et al. [35] proposed a preforming technique in LIW of 0.03 mm thick titanium flyers to 0.1 mm thick copper targets. In this method, a preformed local hump replaced the gap between the foils normally used in LIW. The jetting, springback and wavy interface were all observed similar to other LIW experiments (the preforming method was not explained, but the overall dimensions of the flyer after preforming were provided). In addition, they studied the effect of adding a 0.02 mm thick aluminum foil as an interlayer between the copper flyer and base foils having 0.03 and 0.05 mm thicknesses, respectively [36]. It was reported that the nanoindentation hardness levels increased more in the flyer compared to the target. Lap shearing tests resulted in failure in the upper weld interface (between the flyer and the interlayer).

In following the above review of prior research into general HVIW methods, and LIW in particular, the remainder of this paper is organized as follows: Section 2 describes in detail the experimental setup and materials and methods used to study the effects of incorporating measured spatial and temporal profiles of the laser pulse to better simulate the LIW process. Section 3 contains a comprehensive description of the LIW numerical modeling procedures. The results of modeling and comparisons to the experiments are discussed in Section 4.

2. Experimental Procedures

In the experimental setup, 76.2 mm × 25.4 mm × 3.175 mm borosilicate glass samples, 5 mm × 5 mm × 0.05 mm aluminum alloy 1100 foils, and 10 mm × 10 mm × 0.05 mm 304 stainless steel foils were used as transparent overlay, flyer, and base (target) plates, respectively. A very thin layer of black Rust-Oleum enamel aerosol paint was sprayed on one side of the flyer to serve as a sacrificial ablative layer, preventing the top surface of the flyer from melting. A small thin piece of a clear double-sided tape (slightly larger than the laser spot size) affixed the flyer (from its painted side) to the transparent overlay. Target foils were attached to a fixed metal specimen using clear tape along the opposite edges, as shown in Figure 1. To create a gap as the standoff distance between the metal foils, thin glass coverslips were used as spacers. Standoff distance was controlled by the number of glass coverslips placed between the transparent overlay and the fixed metal specimen. The transparent overlay and the glass spacers were attached to the fixed metal specimen using black tape wrapped around the entire sample on both ends, as shown in Figure 2c. The surface of the metal specimen was covered with black tape to prevent it from bonding with the base foil.

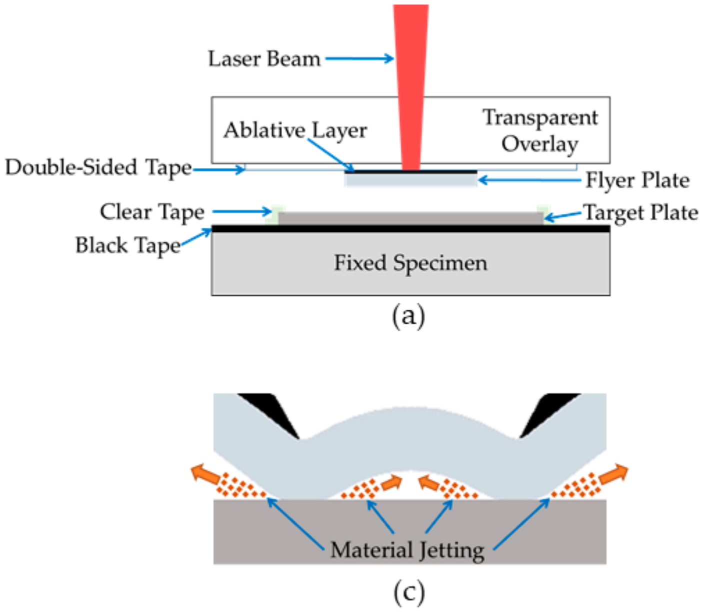

Figure 1. Schematic of the LIW setup and different stages of the experiment: (**a**) LIW components; (**b**) Laser impact; (**c**) Material jetting in the impact region; (**d**) Springback region and welded area. Note: Spacers are not shown.

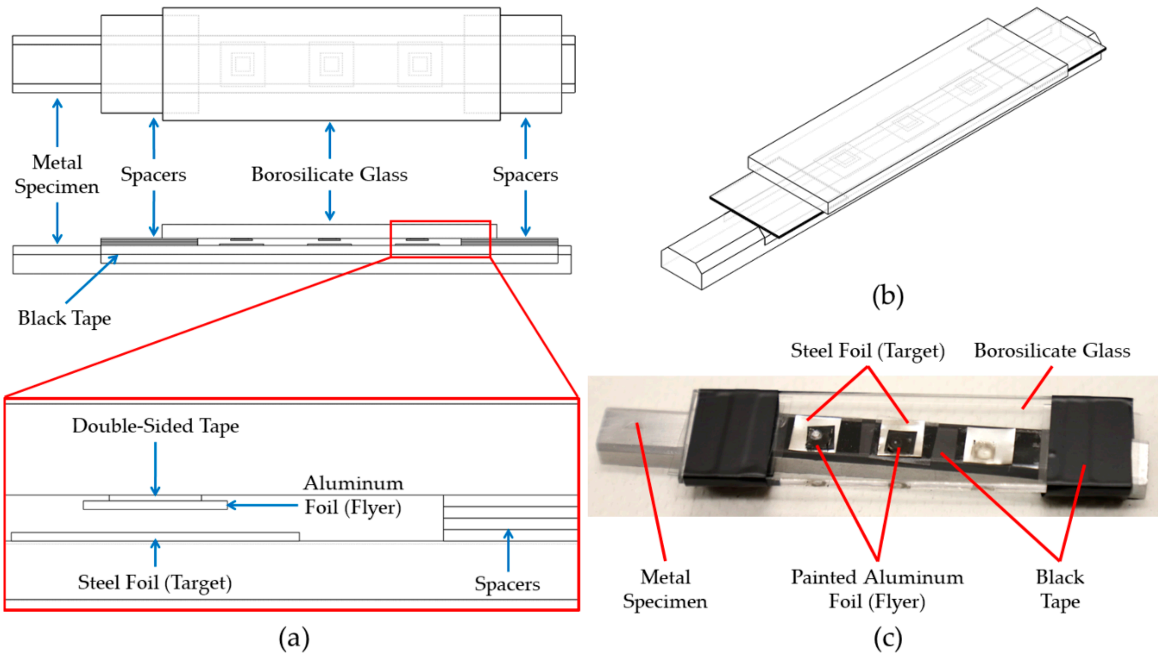

Figure 2. Structure of a LIW specimen: (**a**) Schematic of the LIW specimen (top and side views); (**b**) Schematic of the LIW specimen (isometric view); (**c**) An actual LIW specimen after laser impact.

A Spectra-Physics Quanta Ray Pro-350 infrared laser system (technical specifications listed in Table 1), was utilized for LIW experiments. The laser beam pulse was characterized as depicted in Figure 3. The spatial profile of the laser pulse was measured using an Ophir SP928 high-speed camera utilizing the BeamGage® software. The temporal profile of the laser pulse was measured using an Ophir FPS-1 fast photodetector in conjunction with a Teledyne LeCroy Waverunner 204Xi DSO high-resolution oscilloscope. Measured spatial and temporal profiles of the laser pulse are shown in Figures 4 and 5, respectively.

Table 1. Laser parameters [37,38], with permission from ASME, 2019.

Laser Parameter (Units)	Type/Value(s)
Pulse Type	Q-Switched
Laser Wavelength (nm)	1064
FWHM Pulse Width (ns)	17
Average Pulse Energy (J)	2.5–3 (±2%)
Laser Spot Size (mm)	3.2 ± 0.1
Incident Peak Power Density (GW/cm^2)	1.8–2.2

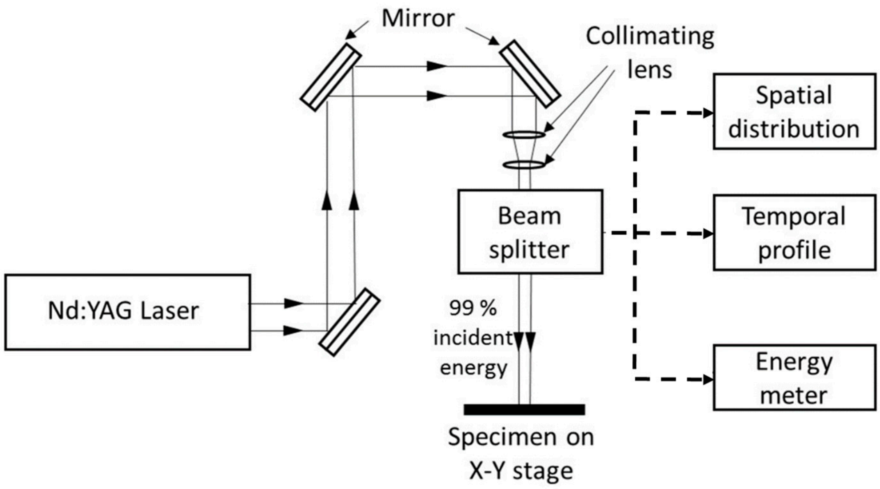

Figure 3. LIW and laser characterization setup. reproduced from [37], with permission from ASME, 2019.

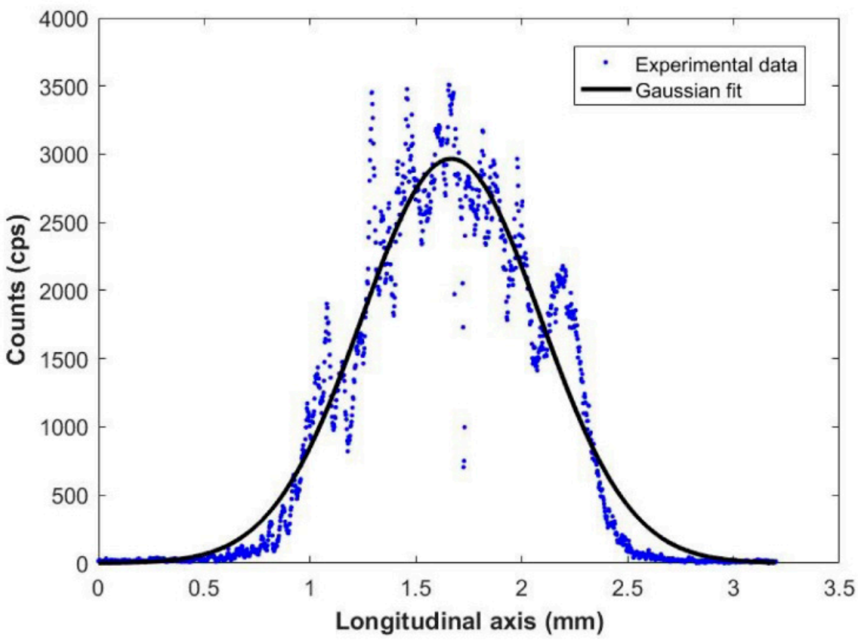

Figure 4. Measured laser pulse spatial profile (assumed axisymmetric) [37,39], with permission from ASME, 2019.

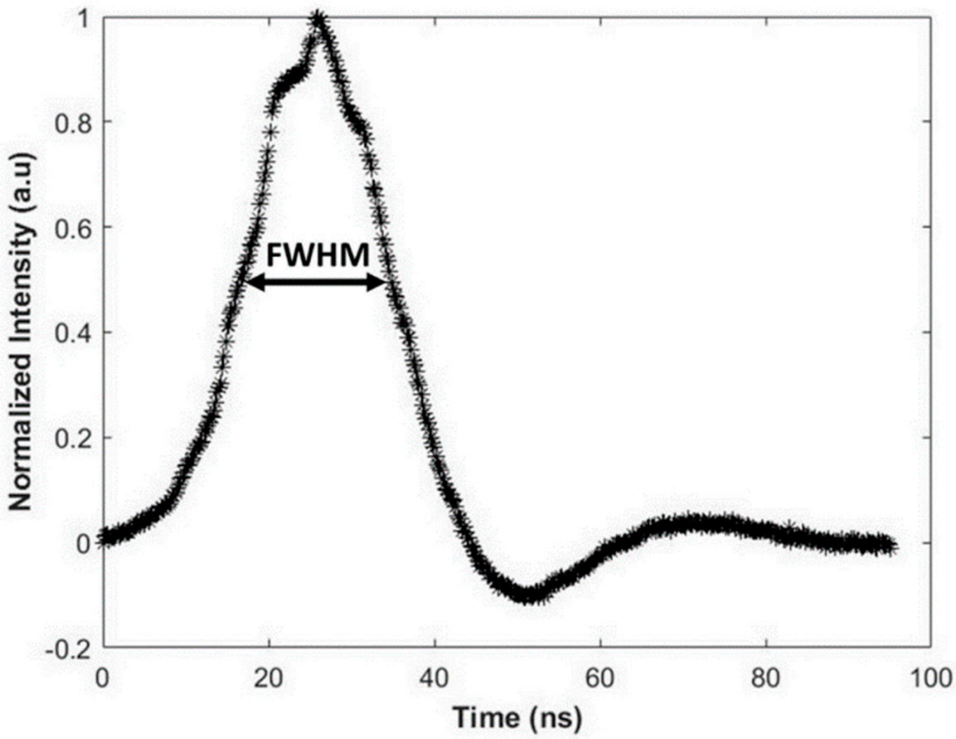

Figure 5. Measured laser pulse temporal profile [37,39], with permission from ASME, 2019.

As can be seen in the earlier Figure 1a, the laser beam passes through the transparent overlay and ablates the sacrificial layer. Since a large amount of energy (2.5–3 J) is released in a very short amount of time (~17 ns) over a small area (0.08 cm^2), the ablative layer reaches extremely high temperatures (above 10,000 °C [40]) and vaporizes instantaneously creating the plasma depicted in Figure 1b. The plasma continues to absorb the energy of the laser and further expands while entrapped in the confinement layer. This leads to the creation of a high-amplitude pressure load penetrating the flyer plate in the form of shock waves. Consequently, the thin flyer plate is launched with high-velocity distribution towards the target plate. In some cases, as reported in the literature [24,30–36], upon collision, bonding is not achieved near the center of the ablated spot since the impact angle is zero and the impact velocity is too great. Instead, the flyer plate (and sometimes also base plate depending on the boundary conditions) springs back. In addition, a jet of metal particles that separates from flyer and base plates is ejected at very high velocities (several thousand m/s), as depicted in Figure 1c. Away from the center point, the impact angle is gradually increased until it reaches the minimum required for a successful weld. Consequently, the welding process initiates and depending on the experimental conditions, flat and/or wavy interfaces can be observed along the weld interface.

After the LIW experiments were performed as described, the welded samples were cut along the centerline of the welds (see Figure 6) and both optical and scanning electron microscope images of the cross-section of the weld were obtained. Prior to cutting, the welded foils were buried in epoxy (poured), wherein the cured epoxy prevented unwanted damage and deformation during the cutting process. After cutting, to reduce the surface roughness of the cut cross-sections, the samples were polished using Allied MetPrep 3™ grinding machine. 6 µm and 1 µm polycrystalline diamond suspensions were used on Gold Label and DiaMat polishing cloths respectively. This was followed by using 0.04 µm colloidal silica suspension on a Final A polishing cloth.

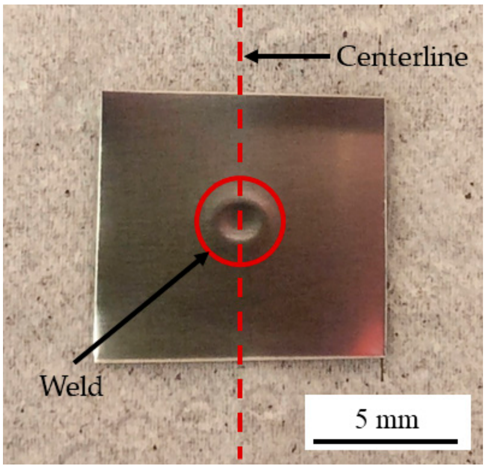

Figure 6. The centerline of the weld.

To measure the strength of the welds, lap shear tests were performed at speed of 0.5 mm/min using a 500 N load cell on an Instron 5969 universal testing system. A schematic of the lap shear test setup is shown in Figure 7. The experimental results are discussed together with the results of the simulations, described next.

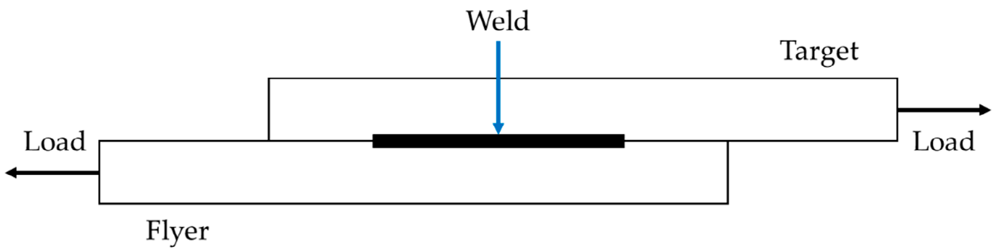

Figure 7. Schematic of the lap shear test.

3. Numerical Simulations

The LIW process, incorporating the spatial and temporal profiles of the laser pulse and its corresponding pressure boundary load, was numerically simulated using two different methods—ALE and Eulerian formulations. As will be shown, these simulations together with the plasma pressure boundary load, provide a more realistic prediction of the LIW process compared to simulations that simply assume an initial constant flyer velocity and flyer shape. In all numerical simulations herein, solution convergence was conducted to determine suitable mesh/grid size. A complete description of the models and techniques used for numerical simulation of the LIW process here is given.

3.1. Plasma Pressure Model

For more realistic simulation of LIW, it is hypothesized that incorporating the transient plasma pressure generated due to laser ablation will provide for improved modeling. Therefore, an axisymmetric Gaussian spatial laser pulse profile (fitted to the measured spatial profile), as well as the measured temporal profile of the laser beam pulse (Figures 4 and 5), were applied in conjunction with the 1D hydrodynamic plasma pressure model by Fabbro et al., which was developed for use in laser shock peening simulation [41]. In this model, during the heating phase, the transient plasma pressure, $P(t)$, is a function of shock impedance Z, plasma thickness $L(t)$, and laser intensity $I(t)$, as shown in Equations (1)–(3).

$$\frac{2}{Z} = \frac{1}{Z_1} + \frac{1}{Z_2}, \tag{1}$$

$$\frac{dL(t)}{dt} = \frac{2P(t)}{Z}, \tag{2}$$

$$I(t) = P(t)\frac{dL(t)}{dt} + \frac{3}{2\alpha}\frac{d[P(t)L(t)]}{dt}, \tag{3}$$

where Z_1 and Z_2 are shock impedances of glass and aluminum, respectively, and α is the fraction of internal energy that dissipates into heat. Coupling Equations (2) and (3) gives Equation (4) [37].

$$\frac{d^2L(t)}{dt^2} = \frac{I(t)}{c_1 L(t)} - \frac{c_1 + c_2}{c_1}\left(\frac{dL(t)}{d(t)}\right)^2 \frac{1}{L(t)}, \tag{4}$$

where $c_1 = \frac{3Z}{4\alpha}$ and $c_2 = \frac{Z}{2}$.

As soon as the laser is switched off (at time t = τ = full width, half maximum (FWHM) of the laser pulse), an adiabatic cooling phase is initiated during which plasma pressure decreases with time as shown in Equation (5).

$$P(t) = P(\tau)\left(\frac{L(\tau)}{L(t)}\right)^{\gamma}, \tag{5}$$

where γ is the adiabatic constant. Parametric constants for modeling of the plasma pressure are listed in Table 2.

Table 2. Parameter values used in plasma pressure modeling [37,42], with permission from ASME, 2019.

Parameter	Magnitude (Units)
Energy ratio (α)	0.25
Adiabatic constant (γ)	1.4
Glass impedance (Z_1)	1.14 (10^6 g/cm^{2}s)
Aluminum impedance (Z_2)	2.75 (10^6 g/cm^{2}s)

Using a substitution, the second-order ordinary differential Equation (4) is rewritten as a system of first-order differential equations and solved numerically using the ode45 solver function in MATLAB® software. Using this solution (in terms of plasma thickness) in Equation (5) and incorporating the measured laser pulse temporal distribution (see Figure 5), the variation of peak plasma pressure over time for an axisymmetric Gaussian spatial pressure was obtained, as shown in Figure 8.

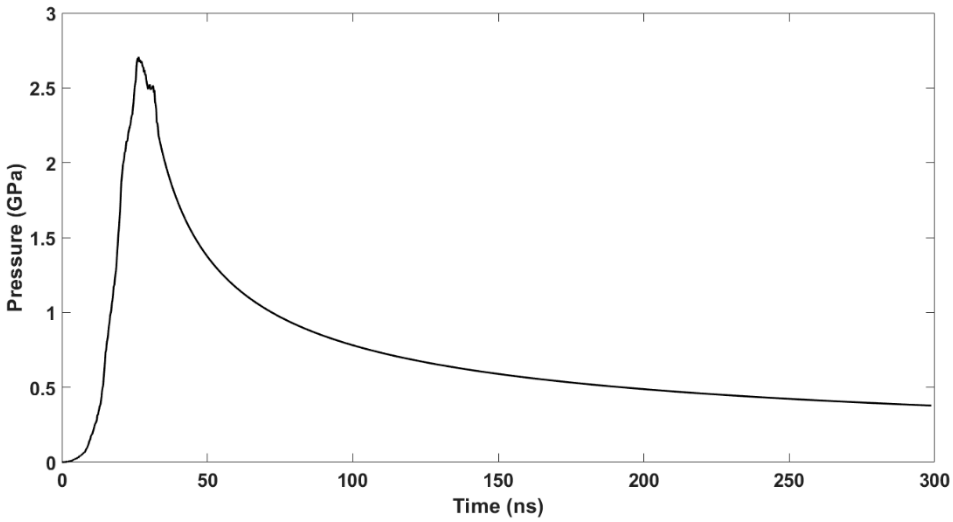

Figure 8. Variation of peak plasma pressure in time.

3.2. Johnson-Cook Model

As a result of very large magnitudes of the pressure load (several GPa) and a very short laser pulse duration (a few ns), extremely high strain rates (over 10^6 s^{-1}) are reached in LIW process, similar to those in laser shock peening. Therefore, the rate-dependent Johnson-Cook (J-C) [43] material constitutive model was implemented to incorporate the effects of strain rate on material behavior. The J-C flow stress (σ_{eq}) is given in Equation (6):

$$\sigma_{eq} = \left(A + B\varepsilon_{eq}^{n}\right)\left[1 + C\,ln\left(\frac{\dot{\varepsilon}}{\dot{\varepsilon}_0}\right)\right]\left[1 - \left(\frac{T - T_0}{T_0 - T_{melt}}\right)^{m}\right], \tag{6}$$

where parameters A, B, n, C, and m are quasi-static yield stress, hardening constant, hardening exponent, strain rate constant, and thermal softening exponent, respectively. These material constants are determined empirically. The rest of the parameters in the J-C model are equivalent plastic strain (ε_{eq}), plastic strain rate ($\dot{\varepsilon}$), reference strain rate ($\dot{\varepsilon}_0$), testing temperature (T), reference temperature (T_0), and melting temperature (T_{melt}). J-C parameters of the materials used are listed in Table 3.

Table 3. J-C parameters [32], with permission from Elsevier, 2019.

Material	A (MPa)	B (MPa)	n	C	m	T_0 (K)	T_m (K)
1100 Aluminum	148.4	345.5	0.183	0.001	0.895	293	916
304 Stainless Steel	110	1500	0.36	0.014	1	293	1673

3.3. Mie-Grüneisen Formulation

To govern the hydrodynamic behavior of the materials, an equation of state (eos) was used, which defines the pressure (of a solid at a given temperature) as a function of the density and the internal energy [44]. The Mie–Grüneisen (M–G) eos was applied to model the materials' volumetric strength at the high pressures present in the LIW process. The M–G eos is a function of energy, relating the shock velocity and the particle velocity. Equations (7)–(14) are found in [44]. The M–G eos is given in Equation (7):

$$P - P_H = \Gamma\rho(E_m - E_H), \tag{7}$$

where P, P_H, Γ, ρ, E_m, and E_H are pressure, Hugoniot pressure, Grüneisen ratio, current density, internal energy per unit mass, and Hugoniot specific energy per unit mass, respectively. The Grüneisen ratio is given in Equation (8):

$$\Gamma = \Gamma_0\frac{\rho_0}{\rho}, \tag{8}$$

where Γ_0 is a material constant and ρ_0 is the density at the reference point. The Hugoniot parameters are functions of density only and are related by Equation (9):

$$E_H = \frac{P_H\eta}{2\rho_0}, \tag{9}$$

where η is the nominal compressive volumetric strain and is given in Equation (10):

$$\eta = 1 - \frac{\rho_0}{\rho}, \tag{10}$$

Replacing the terms in Equation (7) with their definitions in Equations (8)–(10) gives Equation (11):

$$P = P_H\left(1 - \frac{\Gamma_0\eta}{2}\right) + \Gamma_0\rho_0E_m, \tag{11}$$

The Hugoniot pressure is defined through curve fitting to the experimental data and is given in Equation (12):

$$P_H = \frac{\rho_0 c_0^2 \eta}{(1 - s\eta)^2}, \tag{12}$$

where c_0 and s linearly relate the shock velocity (U_s) and particle velocity (U_p) by Equation (13):

$$U_s = c_0 + sU_p, \tag{13}$$

Replacing P_H in Equation (11) with its definition in Equation (12) gives the linear Hugoniot form of the M–G eos in Equation (14):

$$P = \frac{\rho_0 c_0^2 \eta}{(1 - s\eta)^2}\left(1 - \frac{\Gamma_0 \eta}{2}\right) + \Gamma_0 \rho_0 E_m, \tag{14}$$

The M–G eos parameters of the materials used in the simulations are listed in Table 4.

Table 4. M–G eos parameters [31,45], with permission from Elsevier, 2018.

Material	ρ (kg/m^3)	c_0 (m/s)	s	Γ_0
1100 Aluminum	2710	5380	1.337	2.1
304 Stainless Steel	7905	4570	1.490	2.0

The different numerical techniques employed for simulation of the LIW process are described next.

3.4. Axisymmetric LIW Simulation

Due to axisymmetric loading conditions of the laser pulse pressure, an axisymmetric numerical analysis was deemed reasonable for simulation of the LIW process (performed using Abaqus/Explicit software version 16.4-4). The LIW simulation was divided into two steps; during the first step, a pressure load was applied to the flyer as inherited from the measured spatial and temporal profiles of the laser beam pulse. The measured spatial profile was inputted as an analytical field to define the spatial distribution of the pressure load. The measured temporal profile was inputted as the amplitude of the pressure load. This pressure load was applied to the top surface of the flyer and launched it towards the target plate until contact was initiated. In the second step, the flyer collided with the target at a very high-speed profile in the center of the laser impact area, resulting in large deformations. Since large deformations in purely Lagrangian finite elements result in excessive distortion, an ALE domain was utilized in the second step. A meshing frequency of 1 increment, with 50 remeshing sweeps per increment and 50 initial remeshing sweeps were used. About 80,000 4-node axisymmetric, quadrilateral elements of 2.5-micron edge length with bilinear displacement, reduced integration, and hourglass control (CAX4R) were used. The target foil was placed on a fixed analytical rigid body representing the fixed specimen in the LIW setup. In addition, another fixed analytical rigid body was included on top of the flyer foil to act as the fixed transparent overlay. The kinematic contact method was implemented between the foils while the penalty contact method was applied between each foil-rigid body pair (flyer-transparent overlay and target-fixed specimen). The contact interaction property in both the kinematic and the penalty methods was "hard" contact allowing separation after contact. A schematic of the LIW setup in the axisymmetric simulation is shown in Figure 9a. The velocities in different regions of the foils as well as the deformed foil shapes after collision were simulated. Details on the axisymmetric simulation results are provided in Section 4.

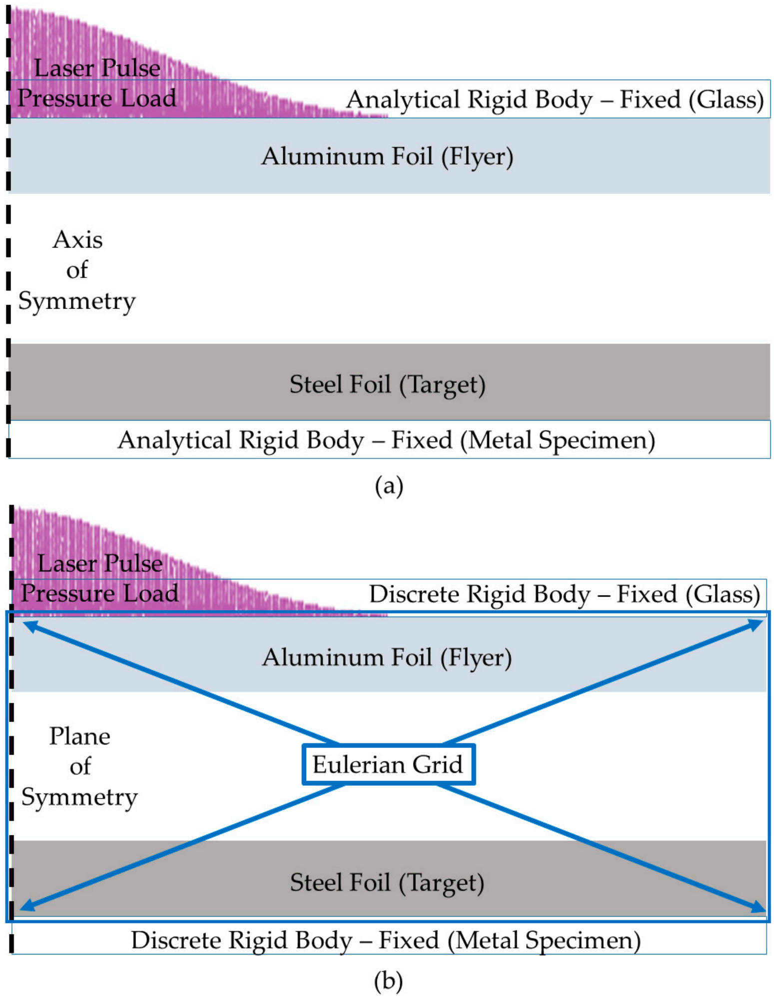

Figure 9. Schematic of the LIW simulations: (**a**) Axisymmetric; (**b**) Eulerian.

3.5. Eulerian LIW Simulation

In order to mimic the material jetting phenomenon, an Eulerian model of the LIW process was run in Abaqus/Explicit. In this model, the material's Eulerian volume fraction (EVF) was computed within each element and its movement was tracked as it flowed through the fixed mesh. A material EVF of one means the element is completely filled with that material while a material EVF of zero shows that the material is not at all present in the element. More than one material may be present in Eulerian elements at the same time. If after adding all the material EVFs in an element, the sum is less than one, the software fills the remainder of the element's volume with "void" material which has zero mass and strength [44]. Since Eulerian models in true 2D space are not available in the particular software, a 3D model was created with a thickness of 0.02 mm (four elements thick) in the out-of-plane (depth) direction. However, motion in the depth direction was constrained by a symmetry condition at all nodes, thus rendering the model an equivalent 2D plane strain simulation (due to plate thicknesses being much smaller than other dimensions). An Eulerian grid (meshed control volume) encompassed the entire model in order to track material movement during LIW. Exploiting symmetry, only half of the full geometry was modeled. Approximately 300,000 hexahedral 8-node Eulerian brick elements of 5-micron edge length with reduced integration and hourglass control (EC3D8R) were utilized, which in turn employed predefined volume fractions at the locations of the flyer and target plates. Two fixed discrete rigid bodies were used as the transparent overlay and the metal specimen. Consistent with an Eulerian model description, Abaqus/Explicit allows for load application only at fixed nodes in the meshed control volume. The pressure load described earlier was applied to the top surface of the flyer based on measured spatial and temporal profiles of the laser pulse. Implementation of the measured spatial and temporal profiles as the distribution and amplitude of the load was similar to that of axisymmetric simulation. The only difference was that the load was apportioned among nodal layers of the initial flyer position in the out-of-plane direction, accelerating the flyer towards the target, resulting in jetting and interlocking of the foils along the weld interface upon collision. The general contact method was implemented between all surface pairs using a "hard" contact interaction property allowing separation after contact. A schematic of the LIW in the Eulerian simulation is shown in Figure 9b. Details on the Eulerian simulation results are provided in Section 4.

4. Results and Discussion

Both experimental and numerical results of this study are presented next. The experimental results are included in form of optical and scanning electron microscope images of the cross-sections of the cut LIW samples. Axisymmetric and Eulerian simulation results are discussed, including advantages and disadvantages of the ALE and Eulerian numerical techniques. The results obtained from numerical simulations are compared with the experimental results, and similarities and discrepancies between them are investigated.

4.1. Experimental Results

Different standoff distances and laser fluence values were used in experiments to acquire the LIW process window. These parameters are listed in Table 5. It was seen that regardless of the tested laser fluence values, standoff distances of 0.12 and 0.54 mm were too small and too large respectively. Successful welds were obtained using standoff distances of 0.26 and 0.40 mm, irrespective of the laser fluence values tested in experiments.

Table 5. List of experimental parameters.

Laser Spot Diameter (mm)	Laser Pulse Energy (J)	Laser Fluence (J/cm^2)	Standoff Distance (mm)	Successful Weld?
3.2	2.5 3.0	31.08 37.30	0.12	No
	2.5 3.0	31.08 37.30	0.26	Yes
	2.5 3.0	31.08 37.30	0.40	Yes
	2.5 3.0	31.08 37.30	0.54	No

Using Leica microscopes, optical images of the weld cross-sections were obtained. Sample images for the case with a laser fluence of 31.08 J/cm^2 and a standoff distance of 0.26 mm are shown in Figures 10 and 11. As mentioned in Section 2, in most LIW experimental results reported in the literature, due to very high flyer impact velocities and very low impact angles, springback occurs and welding is not achieved in the center of the laser-ablated region [24,30–36]. This is an unwanted event which decreases the strength and integrity of the weld. Interestingly, in the experimental results here, the springback phenomenon was not observed in the center of the weld region. As seen in Figure 10, the foils are indeed welded together in the center of impact region, while gaps are observed on the outside of the weld. Figure 11 shows the same weld at two higher magnifications. A combination of flat and wavy interface patterns is observed along the weld interface. Elimination of the springback phenomenon in these experiments could be attributed to the polymeric black tape placed between the target foil and the fixed metal specimen. This tape was used to prevent the target foil from bonding with the metal specimen after laser impact. It is hypothesized that direct placement of the target foil on the metal specimen leads to metal foils (flyer in particular) bouncing off of the specimen after impact resulting in springback at the center of the impact region. It is possible that the addition of a polymer interlayer between the target foil and metal specimen elongates the collision time of the foils, preventing the flyer foil from rebounding (which could lead to springback). The validity of this hypothesis needs to be investigated through further experiments as part of future research.

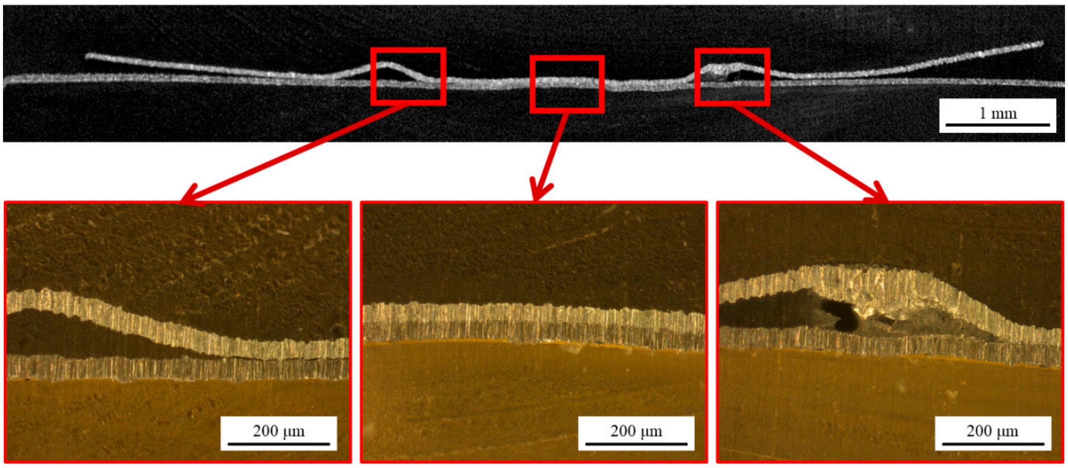

Figure 10. Optical microscope images of different regions of a LIW sample.

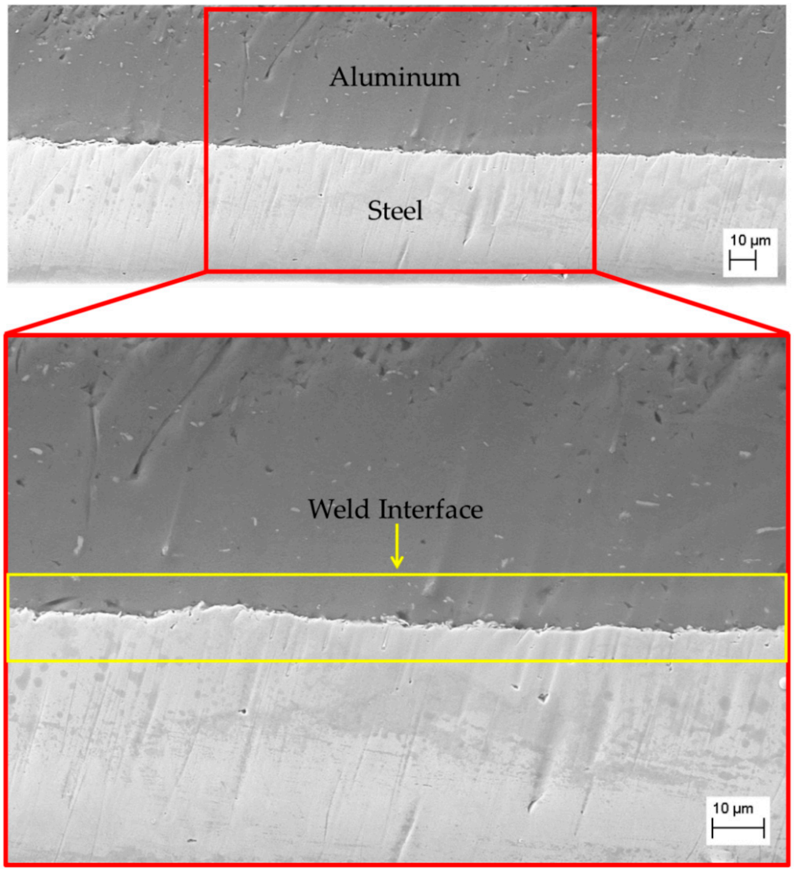

Figure 11. SEM images of a LIW sample at two different magnifications.

Another important observation in these experimental results relates to the overall shape of the welded foils. As seen in Figure 10, while the foils are welded in the central region, there is a gap present on each side of the weld. Since the loading conditions are axisymmetric, this means that the gap has an annular shape. Considering that the experiments include an initial standoff distance between the two foils, and because of the 3D Gaussian profile of the ablation pulse pressure, the generation of a gap that gradually increases with position away from the center of the weld might be expected. However, as seen in Figure 10, starting from the center of the weld, and moving away in the radial direction, the gap gradually increases to a maximum and then starts decreasing, resulting in a shape very similar to the springback region reported in the literature [24,30–36]. Although similar in shape, these are two different phenomena and they happen for different reasons; the annular gap observed in these experiments is attributed to the Gaussian profile of the laser-induced plasma pulse pressure, and the size of the double-sided tape attached to the flyer's laser-ablated area. The double-sided tape is used to enhance the plasma confinement in the glass overlay by eliminating any gap between the flyer foil and the transparent overlay. Due to the Gaussian profile of the pressure load, moving away from the center of the laser-ablated spot in the radial direction, the magnitude of the pressure load decreases significantly. Therefore, if the size of the double-sided tape is considerably larger than that of the laser spot, the laser impact cannot separate the flyer foil from the transparent overlay. In the experiments conducted here, after some trial and error, it was found that a double-sided tape slightly larger than the laser spot resulted in successful plasma confinement and separation of the flyer from the transparent overlay. In the center of the impact area, the flyer detaches from the transparent overlay and is launched towards the target. Away from the center, the resistance of the double-sided tape against separation becomes gradually more significant, together with the decrease in the magnitude of the laser beam pulse pressure. As a result, the size of the gap starts increasing until the edge of the double-sided tape is reached, the flyer is completely detached, and the resistance is no longer present. Subsequently, the gap starts decreasing and then increasing again as the flyer accelerates towards the target.

Lap shear tests were performed on samples with different laser fluences and standoff distances. These results are shown in Figure 12. It was observed that the force linearly increased with displacement until it reached a maximum. Then the weld failed (on the aluminum flyer side) resulting in a sudden drop in force values. Further increasing the displacement resulted in increased tearing of the flyer and thus sliding of the foils. Therefore, the force values gradually decreased until they reached an almost constant value with little change with respect to displacement. Higher fluences resulted in higher maximum force values while increasing the standoff distance decreased the maximum forces.

Numerical results are presented next. Prior to the viewing of numerical results, it is important to note that all experiments were conducted in air at atmospheric pressure. Since the flyer has a supersonic flight, shock waves are generated upon collision of the foils resulting in a strong air-cushion effect. However, the air and its effect on the collision were neglected in the numerical simulations. Therefore, an investigation into the air versus vacuum conditions in the LIW process is a potential area of research as part of future work.

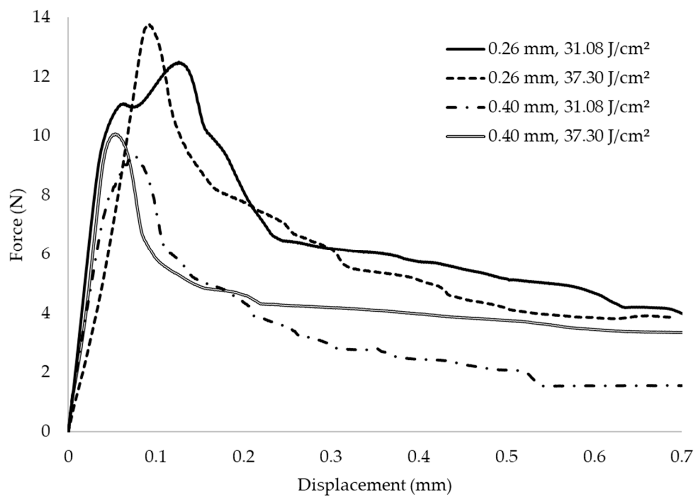

Figure 12. Force-displacement curves obtained from lap shear tests.

4.2. Numerical Results

Axisymmetric ALE and Eulerian numerical methods incorporating the spatial and temporal profiles of the laser beam pressure pulse were implemented in the simulation of the LIW process. In the axisymmetric ALE simulation, the effect of the standoff distance between the foils on the impact angles, nodal velocities, springback, and overall shape of the deformed flyer foil were investigated. Using the Eulerian technique, the jetting phenomenon and the interlocking of the foils along the weld interface were simulated. In addition, the hypothesis that simulation results assuming a constant initial flyer velocity and shape are not as accurate is tested.

The axisymmetric ALE simulation result for the same sample case (laser fluence of 31.08 J/cm^2, and standoff distance of 0.26 mm) is compared to the experimental result, as shown in Figure 13. The diameter of the welded region obtained from experimental and numerical results is 2.5 mm and 2.2 mm, respectively (12% difference). The overall shape of the deformed foils was successfully simulated, showing good agreement with experimental results as seen in Figure 13. Since the effect of the double-sided tape (discussed in experimental results) was neglected, the annular gap observed in the experiments was not fully captured. Therefore, an investigation into the effect of double-sided tape can be pursued in the numerical simulations of the LIW process as part of future research.

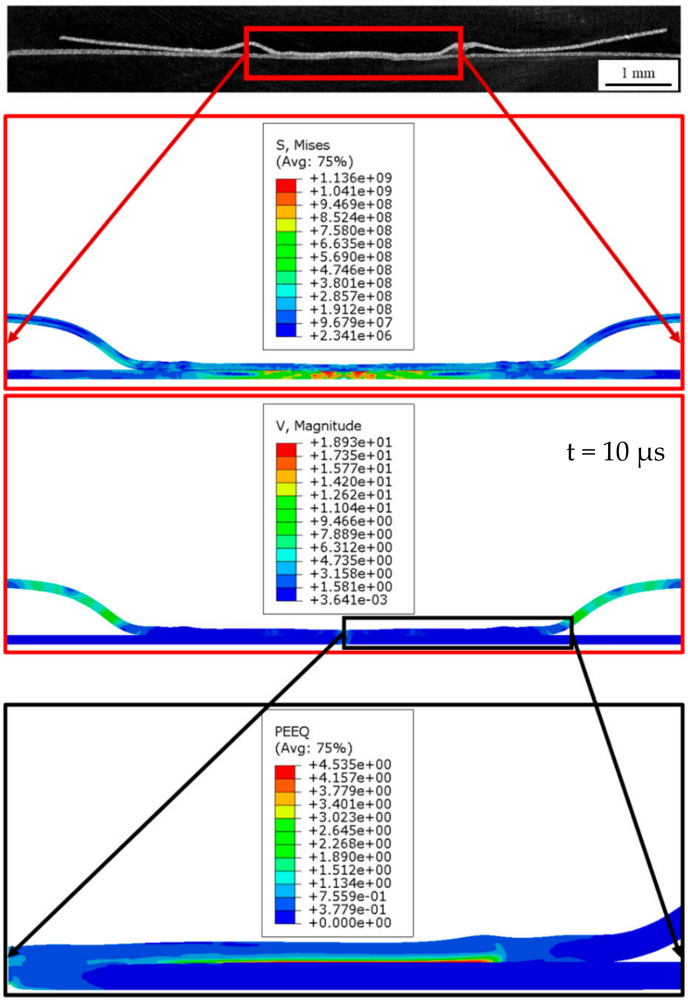

Figure 13. Axisymmetric simulation results: deformed shapes and comparison to experimental results; Contour plots include S: von Mises stress (Pa), V: velocity (m/s), and PEEQ: equivalent plastic strain.

To investigate the importance of the temporal profile of the laser beam pressure pulse, an axisymmetric ALE simulation for a case with a larger standoff distance (0.40 mm) and higher laser fluence (36.06 J/cm^2) was created. The simulation results for this case at different times during the second step of the LIW process are shown in Figures 14 and 15. As seen in these figures, a significant amount of springback is observed. This is due to the fact that the plasma pressure pulse duration (~300 ns, see Figure 8) is significantly shorter than the collision start time (366 ns, see Figures 14 and 15). This means that the pressure load application ends before the flyer collides with the target. Since there is no force to resist the bouncing of the foils, the springback occurs due to the very high flyer velocities (~1550 m/s, see Figure 15) and low impact angles in the center of the impact region.

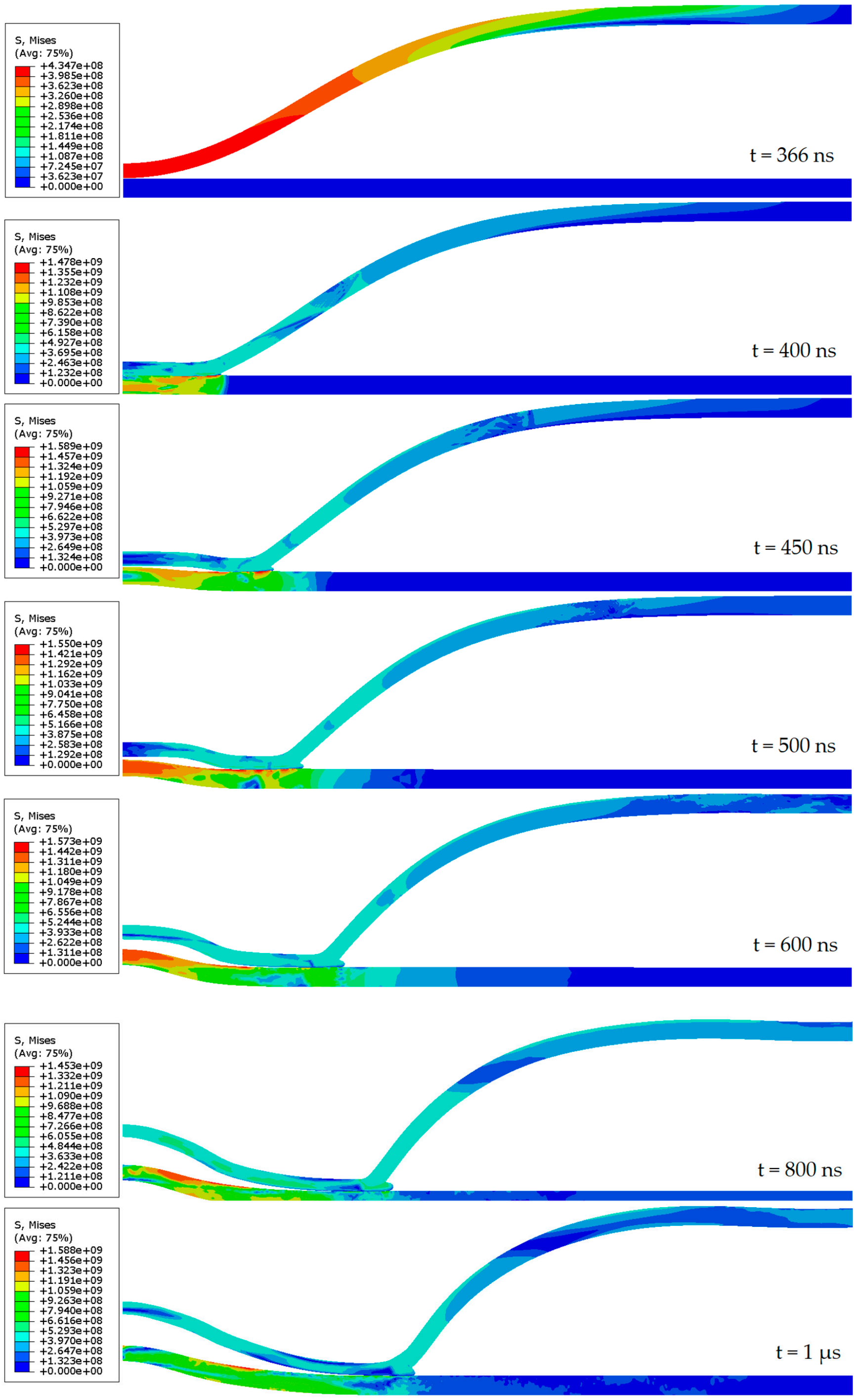

Figure 14. Axisymmetric simulation results: von Mises stress (Pa) contour plot and deformed shape at different times during the collision.

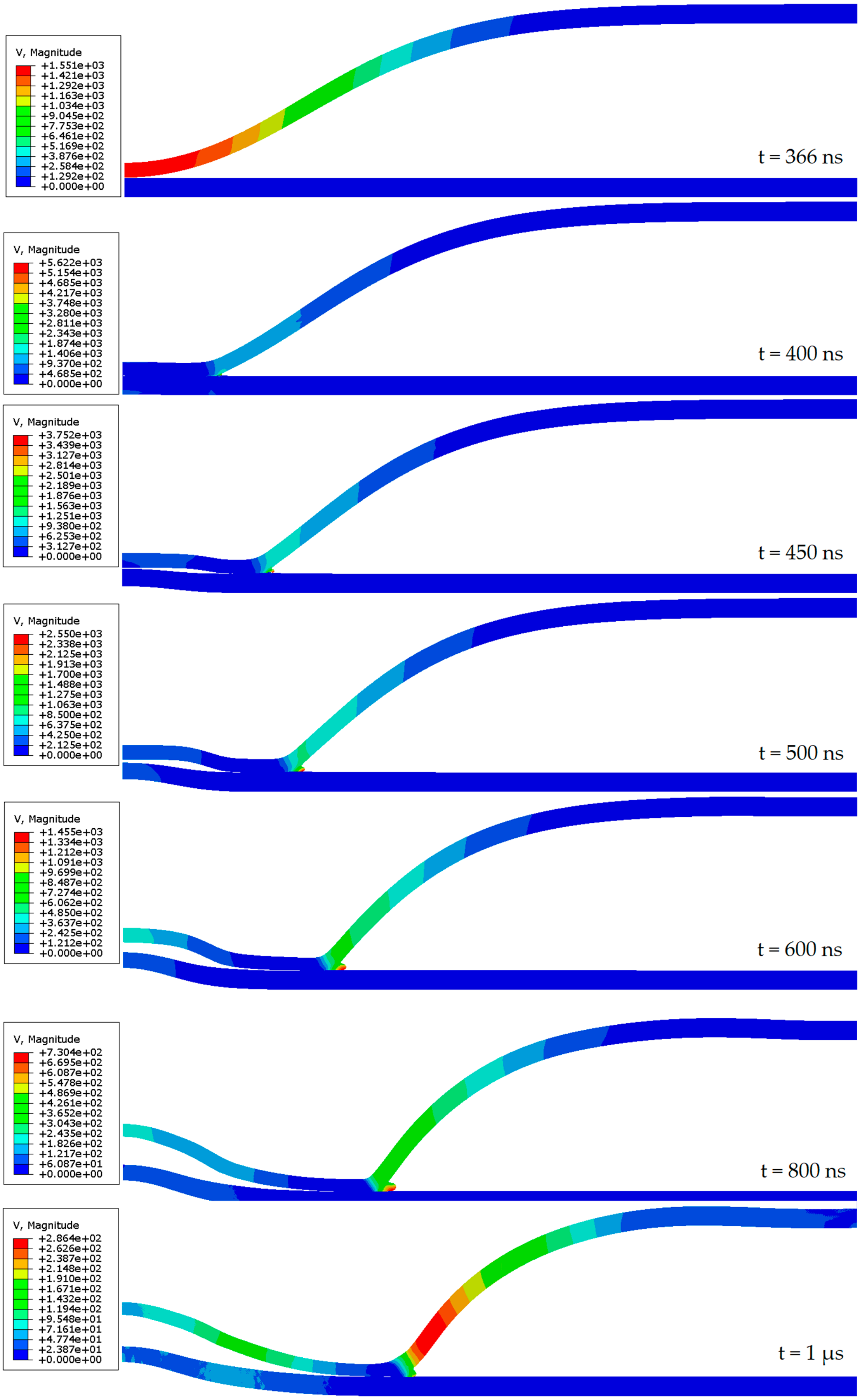

Figure 15. Axisymmetric simulation results: velocity (m/s) contour plot and deformed shape at different times during the collision.

A closer look at the velocities obtained in the collision region (over 5600 m/s, see Figure 16) reveals that jetting velocities were reached in the ALE domain. However, the ALE method is not capable of fully capturing the jetting phenomenon. Note that jetting is one of the known requirements for a successful weld [24,31,32] and happens when metal particles from the foils reach very high velocities upon collision and are ejected from the surface. The resulting 3D images of the deformed foils at 1 µs for this sample case are shown in Figure 17.

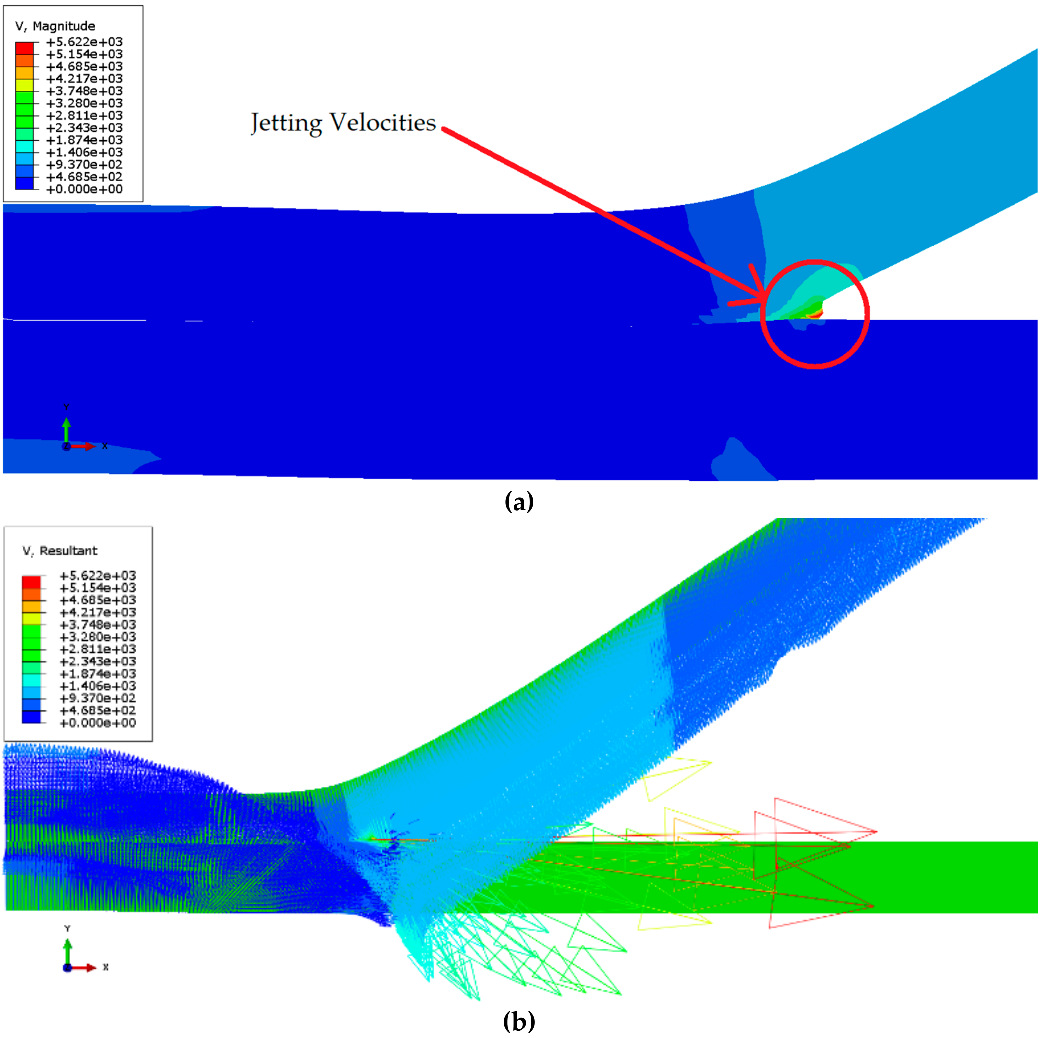

Figure 16. Axisymmetric simulation results at 400 ns: (**a**) Jetting velocities (m/s); (**b**) The resultant velocity vectors in the collision region.

One of the most crucial parameters in the successful execution of LIW is the amount of initial gap between the two foils [25]. If this standoff distance is too small, then the flyer will not have enough time to sufficiently accelerate and/or might not reach the required minimum impact angle before making contact with the base. Conversely, if this gap is too large, the flyer might not reach the base plate or might exceed the maximum required impact angle before the collision with the base. Therefore, it is very important to assess the effect of standoff distance on the impact angles and velocities in different regions of the flyer. The axisymmetric ALE simulation results for sample cases with a laser fluence of 31.08 J/cm^2 and standoff distances from 0.1 mm to 0.4 mm are provided in Table 6.

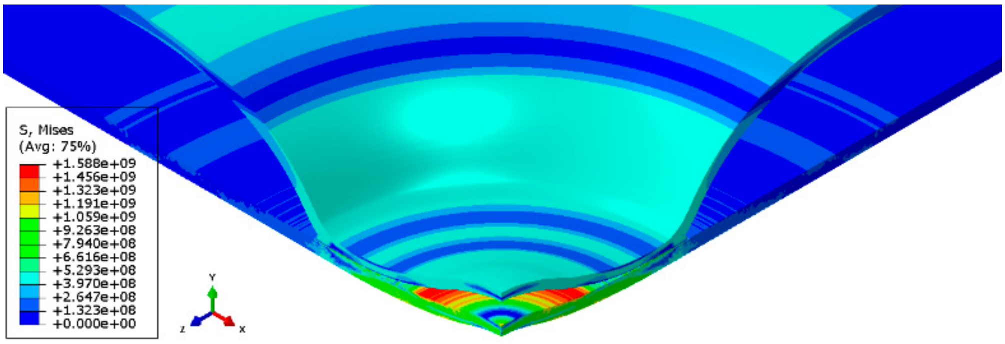

(a)

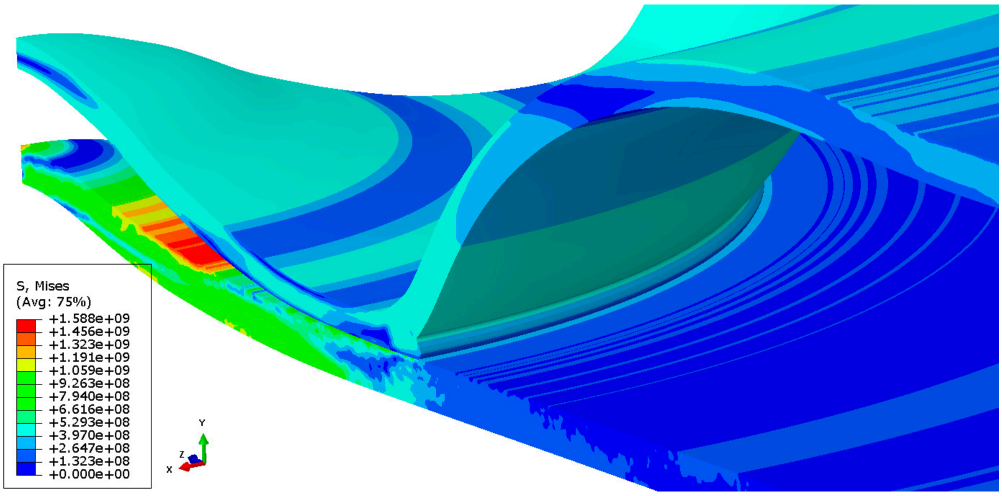

(b)

Figure 17. Resultant 3D images of the deformed foils and von Mises stress (Pa) contour plots (the axysimmetric simulation at 1 μs): (**a**) Overview of the geometry; (**b**) Closer view of the springback.

Table 6. The effect of standoff distance based on axisymmetric LIW simulation.

Standoff Distance (mm)	Maximum Impact Velocity (m/s)	Maximum Impact Angle (degrees)	Collision Time (ns)
0.1	1110	5	146
0.2	1370	15	220
0.3	1580	20	293
0.4	1550	30	366

As mentioned earlier, due to the Gaussian profile of the laser beam, the applied pressure load on the flyer is axisymmetric. Therefore, the resulting impact velocities are maximum in the center of the laser spot and decrease in the radial direction away from the center. Impact angles and velocities at the point of collision for the sample case are shown in Figure 15 (at t = 366 ns). The drastic velocity gradients between different regions of the flyer show the importance of incorporating the spatial profile of the laser beam. As seen in Table 5, the maximum velocity is reached at a distance between 0.3 and 0.4 mm away from the initial flyer position. This means that if the standoff distance is large enough, at a certain time the flyer starts to decelerate, showing the importance of considering the temporal profile of the laser beam. If a constant velocity had been assumed, not only would the changes in accelerations and velocities be ignored over time, but so would the gradients between the different regions of the flyer have been neglected. At the point of collision, starting from the center and moving away radially, the impact angle starts at zero degrees, gradually increases to a maximum, and then slowly decreases back to zero close to the edges of the flyer. This shows that assuming an initial shape or a constant impact angle does not give an accurate representation of the LIW process. To support this claim, two different LIW configurations were simulated using an Eulerian technique applying a constant downward initial flyer velocity of 800 m/s. One assumed an initial flyer impact angle and the other assumed a curved initial flyer shape. These additional simulation results are provided for the sake of comparison with the primary work here in which measured spatial and temporal profiles of the laser beam pulse have been incorporated. As seen in Figure 18, the application of a constant initial velocity results in excessive rebounding of the foils upon collision and is therefore not realistic. Moreover, despite using an Eulerian grid, the jetting phenomenon is not observed at any time during the corresponding LIW simulations.

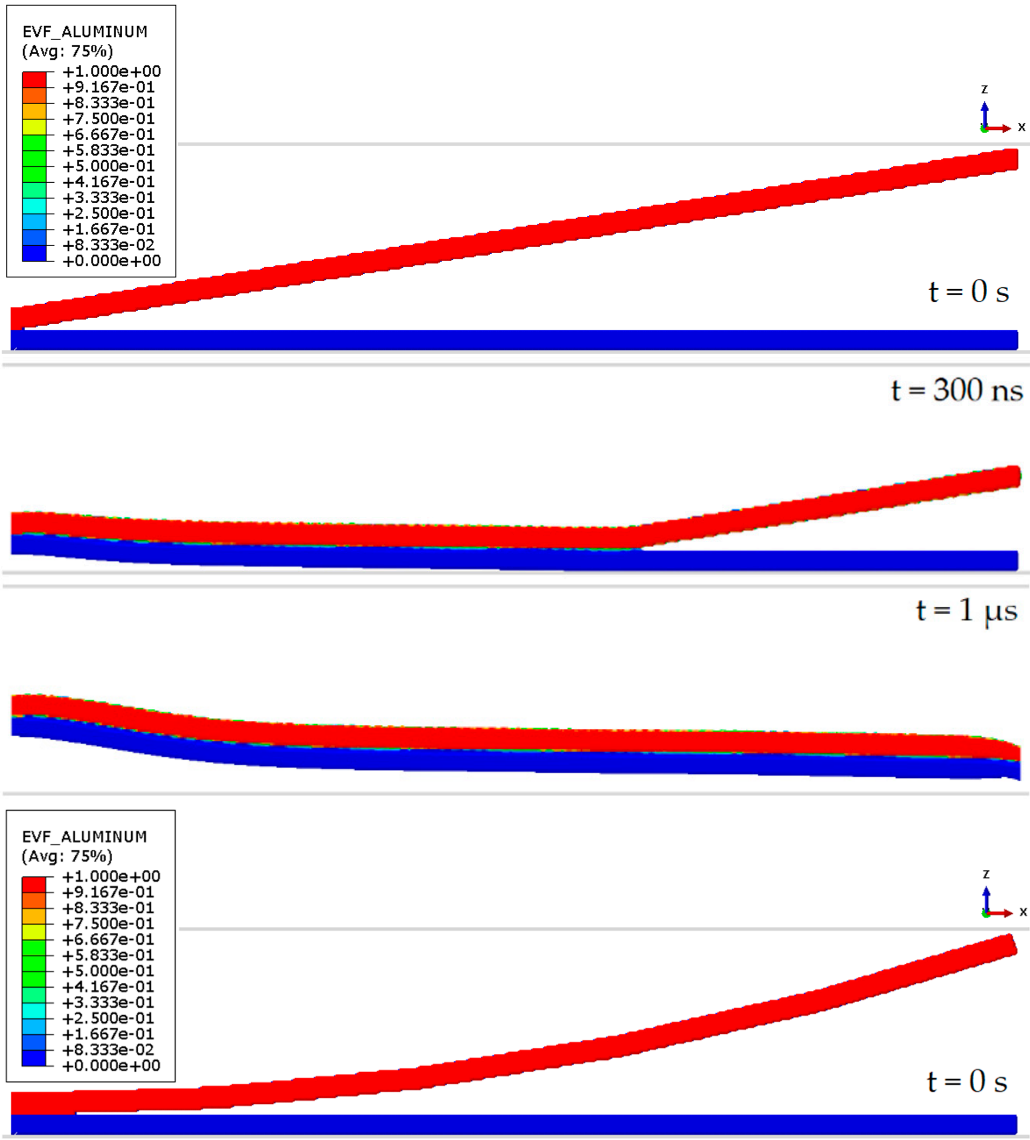

Figure 18. *Cont.*

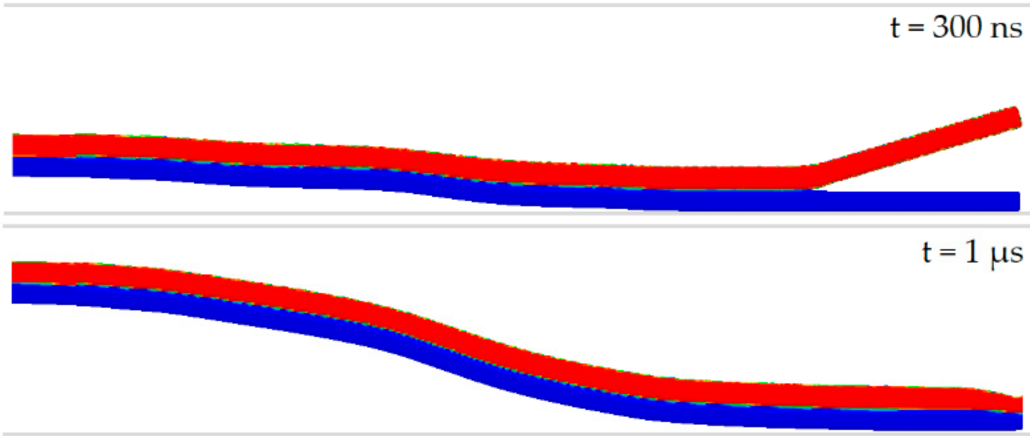

Figure 18. Eulerian volume fraction (EVF) of the aluminum foil in angled and curved LIW orientations at different times in Eulerian simulations assuming an initial flyer shape and constant velocity.

Implementing an Eulerian simulation, the jetting phenomenon and the interlocking of the foils along the weld interface were mimicked. The Eulerian simulation results for a sample case with a 37.30 J/cm^2 laser fluence and a 0.4 mm standoff distance are shown in Figure 19. These results are the volume fraction plots of the aluminum flyer foil. It can be seen that in contrast to some of the reports in the literature [30–32], most of the jet consists of steel target particles. This is despite the fact that aluminum is the softer material compared to steel. Therefore, an experimental investigation into the composition of the jet in the LIW process can be pursued as part of future research.

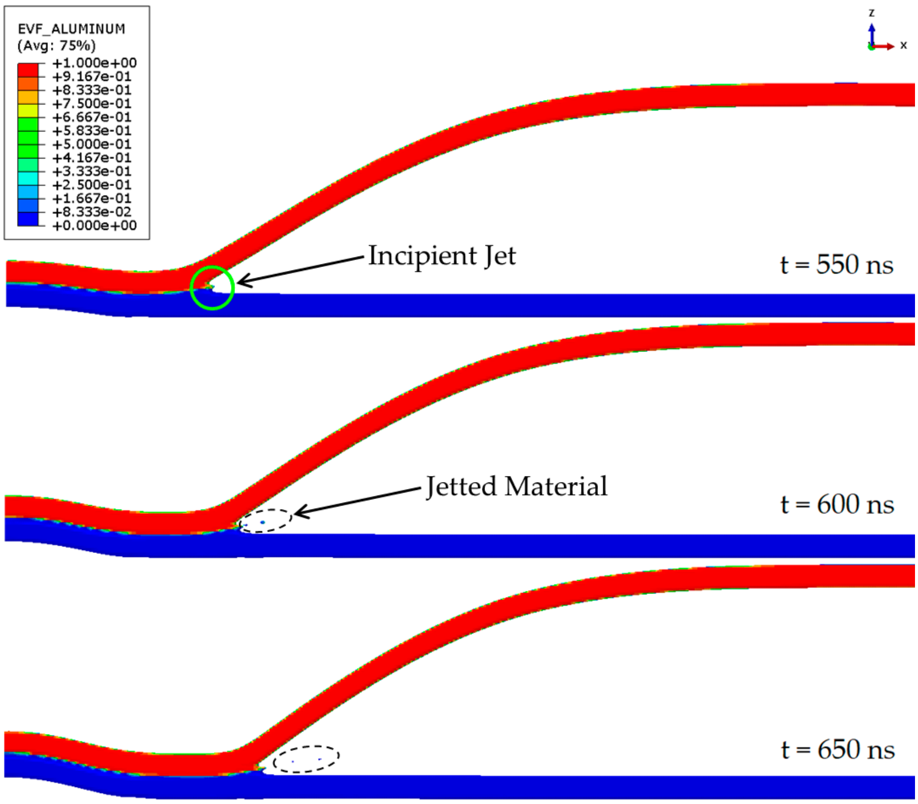

Figure 19. *Cont.*

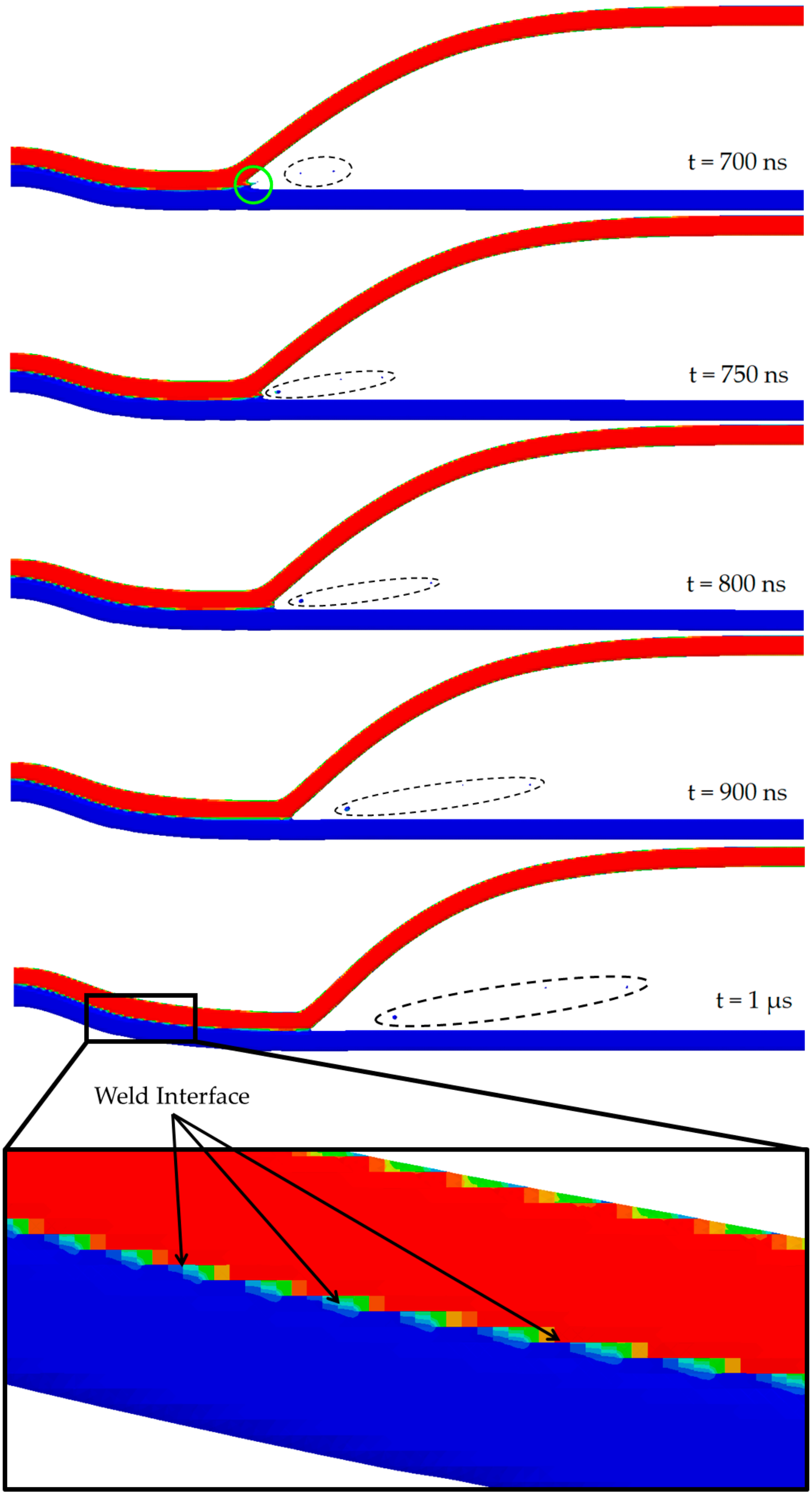

Figure 19. Jetting phenomenon at different times and interlocking of the foils along the weld interface in Eulerian simulation of the LIW process.

As seen in Figure 19, the interlocked foils bounce off in the center of the weld region. This could be attributed to the high fluence of the laser pulse (37.30 J/cm^2) and modeling of the fixed metal specimen as a rigid body, while in reality the metal specimen is made of aluminum. Therefore, the effect of the fixed metal specimen material on rebounding of the foils can also be further studied as part of future research.

5. Conclusions and Future Work

- A more realistic prediction of velocities and deformed shapes in different regions of the foils was achieved through incorporation of the measured temporal and spatial profiles of a Gaussian laser beam pulse pressure, leading to improved simulation of the LIW process in both axisymmetric ALE and Eulerian numerical models.
- LIW experiments were performed using standoff distances of 0.12, 0.26, 0.40, and 0.54 mm, as well as laser fluence values of 31.08 and 37.30 J/cm^2. Irrespective of the laser fluence value, successful welds were obtained only at standoff distances of 0.26 and 0.40 mm.
- Successful welds were obtained without springback in the central region.
- Lap shear test results revealed that the greatest value of maximum force (13.76 N), and thus the strongest weld, was achieved using a standoff distance of 0.26 mm and a laser fluence of 37.30 J/cm^2. In all tests, the failure occurred on the flyer (aluminum) side of the weld.
- Numerical results were compared to experiments, and good agreement was shown between the two.
- The jetting phenomenon and interlocking of the foils along the weld interface were successfully simulated.
- Investigations into the effect of LIW phenomena and factors such as the air medium, jet composition, use of double-sided tape, and the fixed metal specimen material type are deemed as potential topics for future research.

Author Contributions: Conceptualization, S.S.; methodology, S.S., G.H.G., M.I.H., S.F.S. and H.Y.; software, S.S., G.H.G., M.I.H., S.F.S, and H.Y.; validation, S.S.; formal analysis, S.S., G.H.G., S.F.S. and H.Y.; investigation, S.S., G.H.G. and M.I.H.; resources, A.S.M., D.Q.; data curation, S.S.; writing—original draft preparation, S.S.; writing—review and editing, S.S., A.S.M., S.F.S., G.H.G., and H.Y.; visualization, S.S.; supervision, A.S.M.; project administration, A.S.M.; funding acquisition, A.S.M., D.Q.

Funding: This research was funded by The University of Texas at Dallas.

Conflicts of Interest: The authors declare no conflict of interest.

References

1. Crossland, B.; Williams, J.D. Developments in explosive welding. *Aircr. Eng. Aerosp. Technol.* **1968**, *40*, 11–13. [CrossRef]
2. Szecket, A.; Mayseless, M. The triggering and controlling of stable interfacial conditions in explosive welding. *Mater. Sci. Eng.* **1983**, *57*, 149–154. [CrossRef]
3. Mousavi, A.A.; Al-Hassani, S.T.S. Numerical and experimental studies of the mechanism of the wavy interface formations in explosive/impact welding. *J. Mech. Phys. Solids* **2005**, *53*, 2501–2528.
4. Wang, Y.; Beom, H.G. Numerical simulation of explosive welding using the material point method. *Int. J. Impact Eng.* **2011**, *38*, 51–60. [CrossRef]
5. Wang, X.; Zheng, Y. Numerical study of the mechanism of explosive/impact welding using smoothed particle hydrodynamics method. *Mater. Des.* **2012**, *35*, 210–219. [CrossRef]
6. Zhang, Z.L.; Feng, D.L. Investigation of explosive welding through whole process modeling using a density adaptive SPH method. *J. Manuf. Process.* **2018**, *35*, 169–189. [CrossRef]
7. Okagawa, K.; Aizawa, T. Impact seam welding with magnetic pressure for aluminum sheets. *Mater. Sci. Forum* **2004**, *465*, 231–236. [CrossRef]
8. Watanabe, M.; Kumai, S. Interfacial microstructure of magnetic pressure seam welded Al-Fe, Al-Ni and Al-Cu lap joints. *Mater. Sci. Forum* **2006**, *519*, 1145–1150. [CrossRef]

9. Lee, K.J.; Kumai, S. Interfacial microstructure and strength of steel/aluminum alloy lap joint fabricated by magnetic pressure seam welding. *Mater. Sci. Eng. A* **2007**, *471*, 95–101. [CrossRef]
10. Ben-Artzy, A.; Stern, A. Wave formation mechanism in magnetic pulse welding. *Int. J. Impact Eng.* **2010**, *37*, 397–404. [CrossRef]
11. Göbel, G.; Beyer, E.; Kaspar, J. Dissimilar metal joining: Macro-and microscopic effects of MPW. In Proceedings of the 5th International Conference on High Speed Forming, Dortmund, Germany, 24–26 April 2012; pp. 179–188.
12. Raoelison, R.N.; Sapanathan, T. Interfacial kinematics and governing mechanisms under the influence of high strain rate impact conditions: Numerical computations of experimental observations. *J. Mech. Phys. Solids* **2016**, *96*, 147–161. [CrossRef]
13. Cui, J.; Li, Y. Joining of tubular carbon fiber-reinforced plastic/aluminum by magnetic pulse welding. *J. Mater. Process. Technol.* **2019**, *264*, 273–282. [CrossRef]
14. Vivek, A.; Hansen, S.R. Vaporizing foil actuator: A tool for collision welding. *J. Mater. Process. Technol.* **2013**, *213*, 2304–2311. [CrossRef]
15. Hahn, M.; Weddeling, C. Vaporizing foil actuator welding as a competing technology to magnetic pulse welding. *J. Mater. Process. Technol.* **2016**, *230*, 8–20. [CrossRef]
16. Vivek, A.; Presley, M. Solid state impact welding of BMG and copper by vaporizing foil actuator welding. *Mater. Sci. Eng. A* **2015**, *634*, 14–19. [CrossRef]
17. Nassiri, A.; Kinsey, B. Numerical studies on high-velocity impact welding: Smoothed particle hydrodynamics (SPH) and arbitrary Lagrangian–Eulerian (ALE). *J. Manuf. Process.* **2016**, *24*, 376–381. [CrossRef]
18. Nassiri, A.; Zhang, S. Numerical investigation of CP-Ti & Cu110 impact welding using smoothed particle hydrodynamics and arbitrary Lagrangian-Eulerian methods. *J. Manuf. Process.* **2017**, *28*, 558–564.
19. Chen, S.; Daehn, G.S. Interfacial microstructures and mechanical property of vaporizing foil actuator welding of aluminum alloy to steel. *Mater. Sci. Eng. A* **2016**, *659*, 12–21. [CrossRef]
20. Chen, S.; Huo, X. Interfacial characteristics of Ti/Al joint by vaporizing foil actuator welding. *J. Mater. Process. Technol.* **2019**, *263*, 73–81. [CrossRef]
21. Gupta, V.; Lee, T. A robust process-structure model for predicting the joint interface structure in impact welding. *J. Mater. Process. Technol.* **2019**, *264*, 107–118. [CrossRef]
22. Groche, P.; Becker, M. Process window acquisition for impact welding processes. *Mater. Des.* **2017**, *118*, 286–293. [CrossRef]
23. Daehn, G.S.; Lippold, J.C. Low-Temperature Spot Impact Welding Driven without Contact. U.S. Patent No. PCT/US09/36499, 27 December 2011.
24. Wang, H.; Liu, D.; Taber, G. Laser Impact Welding-Process Introduction and Key Variables. Available online: https://eldorado.tu-dortmund.de/bitstream/2003/29542/6/Wan12.pdf (accessed on 7 October 2019).
25. Wang, H.; Taber, G. Laser impact welding: Design of apparatus and parametric optimization. *J. Manuf. Process.* **2015**, *19*, 118–124. [CrossRef]
26. Wang, H.; Vivek, A. Laser impact welding application in joining aluminum to titanium. *J. Laser Appl.* **2016**, *28*, 032002. [CrossRef]
27. Levieil, B.; Bridier, F. Numerical simulation of low-cycle fatigue behavior of welded joints for naval applications: Influence of residual stresses. *Weld. World* **2017**, *61*, 551–561. [CrossRef]
28. Wang, X.; Gu, C. Laser shock welding of aluminum/aluminum and aluminum/copper plates. *Mater. Des.* **2014**, *56*, 26–30. [CrossRef]
29. Peyre, P.; Berthe, L.; Fabbro, R. Laser shock processing of materials: Basics mechanisms and applications. In Proceedings of the 65th Laser Materials Processing Conference, Tokyo, Japan, 2–5 December 2005; pp. 95–109.
30. Wang, X.; Gu, Y. An experimental and numerical study of laser impact spot welding. *Mater. Des.* **2015**, *65*, 1143–1152. [CrossRef]
31. Wang, X.; Shao, M. Numerical simulation of laser impact spot welding. *J. Manuf. Process.* **2018**, *35*, 396–406. [CrossRef]
32. Wang, X.; Li, F. Experimental and numerical study on the laser shock welding of aluminum to stainless steel. *J. Opt. Lasers Eng.* **2019**, *115*, 74–85. [CrossRef]
33. Wang, X.; Shao, M. Laser impact welding of aluminum to brass. *J. Mater. Process. Technol.* **2019**, *269*, 190–199. [CrossRef]
34. Wang, X.; Luo, Y. Experimental investigation on laser impact welding of Fe-Based amorphous alloys to crystalline copper. *Materials* **2017**, *10*, 523. [CrossRef]

35. Liu, H.; Gao, S. Investigation on a novel laser impact spot welding. *Metals* **2016**, *6*, 179. [CrossRef]
36. Liu, H.; Jin, H. Investigation on Interface Morphology and Mechanical Properties of Three-Layer Laser Impact Welding of Cu/Al/Cu. *Metallur. Mater. Trans. A* **2019**, *50*, 1273–1282. [CrossRef]
37. Hatamleh, M.I.; Mahadevan, J. Prediction of Residual Stress Random Fields for Selective Laser Melted A357 Aluminum Alloy Subjected to Laser Shock Peening. *ASME J. Manuf. Sci. Eng.* **2019**, *141*, 101011. [CrossRef]
38. Hatamleh, M.I.; Sadeh, S.; Farooq, T. Finite Element Study of Laser Peening on Selective Laser Melted A357 Aluminum Alloy During Tension Test. In Proceedings of the ASME 2018 13th International Manufacturing Science and Engineering Conference, College Station, TX, USA, 18–22 June 2018; p. V004T03A046.
39. Mahadevan, J.S. Probabilistic Material Modeling of Selective Laser Melted A357 Aluminum Alloy Subjected to Laser Shock Peening. Master's Thesis, University of Texas at Dallas, Richardson, TX, USA, 2017.
40. Ding, K.; Ye, L. 1 General introduction. In *Laser Shock Peening: Performance and Process Simulation*; Woodhead Publishing: Cambridge, UK, 2006; p. 2.
41. Fabbro, R.; Fournier, J. Physical study of laser-produced plasma in confined geometry. *J. Appl. Phys.* **1990**, *68*, 775–784. [CrossRef]
42. Hong, X.; Wang, S.B. Confining medium and absorptive overlay: Their effects on a laser-induced shock wave. *J. Opt. Lasers Eng.* **1998**, *29*, 447–455. [CrossRef]
43. Johnson, G.R.; Cook, W.H. Fracture characteristics of three metals subjected to various strains, strain rates, temperatures and pressures. *Eng. Fract. Mech.* **1985**, *21*, 31–48. [CrossRef]
44. Dassault Systèmes. *Abaqus Analysis User's Guide, v6.14*; Dassault Systèmes: Waltham, MA, USA, 2014.
45. Altair Engineering Inc. *Radioss Theory Manual, v14*; Altair Engineering Inc.: Troy, MI, USA, 2015.

© 2019 by the authors. Licensee MDPI, Basel, Switzerland. This article is an open access article distributed under the terms and conditions of the Creative Commons Attribution (CC BY) license (http://creativecommons.org/licenses/by/4.0/).